OPTICA

Enhanced spin–orbit coupling in an epsilon-near-zero material

Jörg S. Eismann,[1,2,3] Lisa Ackermann,[2] Brian Kantor,[1] Sergey Nechayev,[2] M. Zahirul Alam,[4] Robert Fickler,[4,5] Robert W. Boyd,[4,6,7] and Peter Banzer[1,2,3,7,*]

[1]Institute of Physics, University of Graz, NAWI Graz, Universitätsplatz 5, 8010, Graz, Austria
[2]Max Planck Institute for the Science of Light, Staudtstr. 2, D-91058 Erlangen, Germany
[3]Institute of Optics, Information and Photonics, University Erlangen-Nuremberg, Staudtstr. 7/B2, D-91058 Erlangen, Germany
[4]Department of Physics, University of Ottawa, Ottawa, Ontario K2P 2M8, Canada
[5]Photonics Laboratory, Physics Unit, Tampere University, Tampere, FI-33720, Finland
[6]The Institute of Optics, University of Rochester, Rochester, New York 14627, USA
[7]Max Planck-University of Ottawa Centre for Extreme and Quantum Photonics, 25 Templeton St., Ottawa, Ontario K1N 6N5, Canada
*Corresponding author: Peter.Banzer@uni-graz.at

Received 28 June 2022; revised 16 August 2022; accepted 17 August 2022; published 19 September 2022

Light can carry both spin and orbital angular momentum. While it is known that a nonparaxial circularly polarized beam couples the spin angular momentum to orbital angular momentum, this phenomenon does not hold upon collimation of the field. With the rising interest in epsilon-near-zero photonics, integral ingredients to this field are the beam-shaping capabilities of such a regime. In this work, it is experimentally shown that a permanent conversion of spin-to-orbital angular momentum arises naturally from an incident circularly polarized field on an isotropic interface due to the asymmetry in the Fresnel coefficients. More significantly, the conversion efficiency can be substantially enhanced in the presence of an epsilon-near-zero film due to the unique Fresnel properties exhibited in such a regime. It is further shown that the conversion efficiency scales with the nonparaxiality of the incident field. Our study showcases the intriguing phenomena resulting from the combination of concepts as old as Fresnel coefficients and modern materials such as epsilon-near-zero films.

https://doi.org/10.1364/OPTICA.469079

1. INTRODUCTION

A circularly polarized photon carries spin angular momentum of $\pm\hbar$ due to the nature of the electric field vector. In addition, a spatially structured photon with a helical phase front can carry orbital angular momentum (OAM) of $\pm l\hbar$, where l is the integer number of windings in the phase front [1–3]. When considering a Gaussian beam with uniform circular polarization, the polarization and spatial degrees of freedom of the beam are taken to be decoupled in standard paraxial optics. Therefore, when one changes the polarization of such a beam using a half-wave plate, the spatial mode does not change. However, when light interacts with wavelength-scale inhomogeneities of a material, or if it propagates in a nonparaxial fashion, the spin degree of freedom can couple to OAM and thus to the spatial structure of a light field. This effect is somewhat analogous to the spin–orbit interaction of electrons in a solid and is known as the spin–orbit interaction of light [4–7]. In general, spatial modes of light have been used to probe fundamental light–matter interactions, which has led to the finding of a number of promising applications in classical and quantum optics including optical manipulation, trapping, superresolution imaging, high dimensional quantum information, selective excitation of modes in nanoparticles, etc. [2,6,8–16]. A light beam carrying OAM can be generated by various methods: cavities, astigmatic lenses, forked holograms, spiral phase plates, and spatial light modulators [17–21]. These techniques rely on introducing a phase discontinuity in the wavefront and do not necessarily depend on the polarization of the input light beam. In contrast, structures made of Berry phase elements—such as q-plates, dielectric or plasmonic metasurfaces, and holograms—can be used to convert a beam carrying spin angular momentum into a beam carrying OAM [22–25]. Furthermore, spin–orbit interactions commonly occur in the Fourier spectrum of nonparaxial circularly symmetric focal fields [26–29]. This effect of nonparaxial OAM generation is, however, lost upon collimation. Finally, spin–orbit interactions can also show up for circularly polarized beams impinging on planar unstructured interfaces [30–32]. By utilizing the spin–orbit interaction brought on by an incident circularly polarized field interacting with a planar interface, the generated OAM can be retained after collimation and observed in the far field.

In this paper, we experimentally show that the spin–orbit coupling of a circularly polarized beam incident on a planar interface is strengthened in an epsilon-near-zero (ENZ) environment by simply exploiting the Fresnel coefficients present in such a setting. ENZ materials have become increasingly attractive recently due

to their extreme nonlinear optical properties and their compatibility with photonic integrated circuits [33–35]. We show that the permanent conversion from a homogeneous circularly polarized beam, of left or right handedness, to a circularly polarized OAM mode of opposite handedness with $l = \pm 2$ occurs due to the polarization-dependent asymmetry in Fresnel coefficients. It is further demonstrated that the conversion efficiency for such a process scales with the nonparaxiality of the incident field, and that the process remains efficient for a suitable range of wavelengths above the ENZ wavelength. The measurements are performed for two materials: one being a simple uncoated glass coverslip and the other an ENZ film on a glass substrate. The bare glass coverslip allows us to demonstrate that this spin–orbit interaction is a general phenomenon occurring for arbitrary interfaces while also serving as a baseline to compare the conversion efficiency with respect to an ENZ environment. The experimental setup, described in more detail below, utilizes the cylindrical symmetry shared between the incident beam and a high numerical aperture (NA) objective that focuses the field onto the planar interface. The transmitted field is collected by a high NA oil immersion objective where the beam is then decomposed into its fundamental mode and the generated OAM mode.

2. FRESNEL COEFFICIENTS AND SPIN–ORBIT COUPLING

The behavior of light at an interface is determined by the complex values of the relative permittivities (ϵ) and the relative permeabilities (μ) of materials on both sides of the interface. At optical frequencies, a nonmagnetic material has unit permeability, and thus the values of the relative permittivities of the two materials primarily dictate the light–matter interactions at the interface. Over the past two decades, there has been growing interest in understanding and utilizing the light–matter interaction in materials with vanishingly small permittivities, otherwise known as ENZ materials. Such a material has a permittivity value that lies between $(-1 < \mathrm{Re}(\epsilon) < 1)$. In general, the permittivity of a material is a complex number, and if the imaginary part is small while the real part is zero or near zero, the refractive index is also near zero ($n = \sqrt{\epsilon}$). Consequently, the wavelength ($\lambda = \lambda_0/n$) inside the medium gets stretched, the phase velocity ($v = c/n$) diverges, and the electric field becomes spatially "static-like" over the entire material while oscillating in time. ENZ materials allow tunneling of electromagnetic waves through deep subwavelength narrow channels and arbitrary bends, enhance the directivities of antennas, and lead to strong nonlinear light–matter interactions [36–40]. The exotic properties of ENZ materials further enable the boundary conditions for an air–ENZ semi-infinite system to produce significant contrasts in the Fresnel coefficients for incident TE and TM fields. In particular, the complex Fresnel transmission coefficient t_{TM} scales considerably with both n and ϵ, whereas t_{TE} in comparison has only a minor dependence [41]. In the ENZ framework, where $\mathrm{Re}(\epsilon) \simeq 0$ and $n < 1$, a substantial contrast occurs between the two Fresnel coefficients which, as will be shown later, leads to more efficient spin–orbit coupling. Throughout this paper, a 310 nm thick indium tin-oxide (ITO) film on top of a BK7 glass substrate will be used as the ENZ environment [39]. ITO is a transparent conducting oxide whose permittivity can be modeled following the Drude formula in the near-infrared range. Ellipsometry data were recorded for the ITO film used in our experiments (Fig. 1) to find the ENZ wavelength, which turned out to be $\lambda = 1240$ nm.

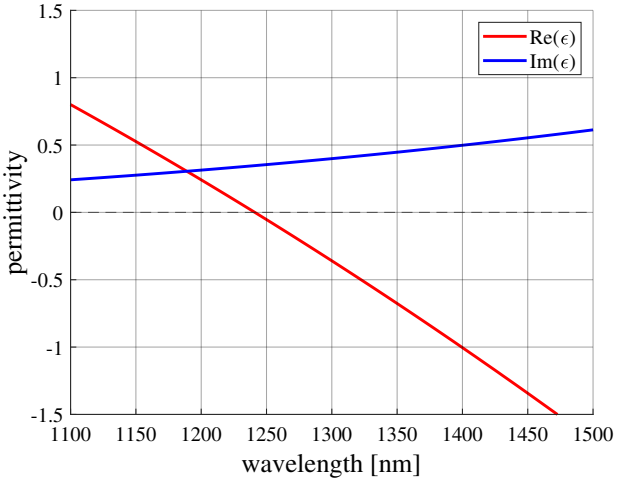

Fig. 1. Permittivity of a 310 nm thick ITO film recorded with ellipsometry measurements. The zero crossing of $\mathrm{Re}(\epsilon)$ occurs around $\lambda = 1240$ nm, with a nonzero imaginary component of roughly $\mathrm{Im}(\epsilon) = 0.37$.

The spin–orbit interaction of a circularly polarized Gaussian beam incident on a planar interface can be understood by considering the distribution of wave vectors comprising the beam (Fig. 2). In the case of transmission, these wave vectors experience both complex Fresnel transmission coefficients t_{TE} and t_{TM} [Fig. 2(a)]. These coefficients unbalance the amplitude ratio of the TE and TM field components while also performing a rotation (phase delay) owing to their complex nature [Fig. 2(b)]. The same phenomenon appears for other wave vectors of the angular spectrum created by the cylindrically symmetric focusing objective [Fig. 2(c)]. Since $t_{\mathrm{TE}} = t_{\mathrm{TM}}$ for normal incidence, the center of the

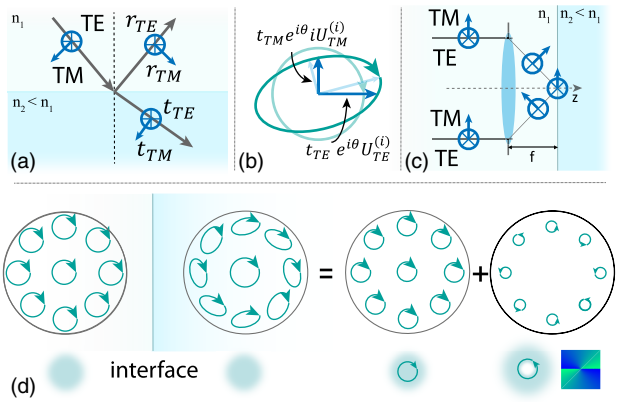

Fig. 2. (a) Reflection and transmission for TE and TM components. (b) Calculation of transmitted field: field amplitudes $U^{(i)}_{\mathrm{TE}}$ and $U^{(i)}_{\mathrm{TM}}$ are scaled with corresponding Fresnel coefficients and propagator. Due to the intrinsic difference of $t_{\mathrm{TE}} \neq t_{\mathrm{TM}}$, the circular polarization becomes skewed elliptically, and the principal axis rotates. Shown here for the case of transmission. (c) For a given plane of incidence, TE and TM field components are affected differently when focused. (d) After transmission through or reflection at an interface, polarization ellipses change according to cylindrical symmetry of the system. In the circular basis, the field is shown as a superposition of left- and right-handed beams, where the generated OAM mode carries the opposite handedness of the incident beam. As a consequence of angular momentum conservation, the converted field possesses an OAM of order two.

beam remains circularly polarized with its initial handedness. In the circular polarization basis, the transmitted elliptically polarized field distribution can be decomposed into two superimposed fields of right and left handedness. Therefore, in the case of an incident right-hand circularly polarized (RCP) beam, the transmitted elliptically polarized field is a combination of the incident RCP Gaussian beam and the converted left-hand circularly polarized (LCP) OAM beam [Fig. 2(d)].

The symmetry of the system enforces that the converted beam must carry a topological charge of $l = \pm 2$. This is understood when realizing that for a given plane of incidence on the interface, wave vectors opposite of each other with respect to the optical axis share the same angle of incidence and polarization. These wave vectors therefore interact with equivalent Fresnel coefficients and consequently experience the same phase. Furthermore, TE and TM polarization components are defined relative to the plane of incidence, which rotates with the azimuthal position in the aperture of the focusing system. A similar effect can also be realized in the inverse setting, where the medium itself possesses a geometry such that the Fresnel coefficients vary by the angle of the structure, rather than the angle of the incident wave vector. This has been experimentally explored with glass cones, where incident paraxial beams with various polarization profiles reflect off the conical glass interface and experience a dephasing between the TE and TM components. In such a system, a variety of polarization-structured beams with helical phase fronts can be produced [42].

Since the spin–orbit interaction in our case is governed by Fresnel coefficients, the predominance of the generated OAM is dependent on how strongly t_{TE} and t_{TM} contrast with one another [43]. Therefore, the stronger the difference in Fresnel coefficients the more efficient the spin–orbit interaction becomes. To maximize this effect, one can take advantage of an ENZ environment that offers such a disparity in Fresnel coefficients. In addition to this, a high NA objective, which tightly focuses the incident beam, can be used. By increasing the nonparaxiality of the incident field with a high NA objective, a stronger contribution from the differing Fresnel coefficients can be realized, and the amplitude of the converted OAM mode scales accordingly.

3. RESULTS

Figure 3(a) shows the experimental setup. A linearly polarized beam from a supercontinuum source that is spectrally filtered is sent through a beam splitter and a liquid crystal variable retarder to produce circular polarization of either left or right handedness. The component reflected from the beam splitter serves as a reference beam. A high NA (NA = 0.9) microscope objective was used to tightly focus the Gaussian beam onto the target sample. When working around the ENZ wavelength, the objective enables tight focusing of the beam to roughly a micrometer spot size in air. The transmitted light is collected with a high NA = 1.3 oil immersion microscope objective in confocal alignment to collimate the output beam. A liquid crystal retarder is used to convert each circular polarization component to a linear basis, i.e., vertical or horizontal polarizations. A beam splitter then combines both the transmitted linearly polarized beam and the linearly polarized reference beam such that their interference can be measured. The far-field patterns and the angular spectra for both the converted and non-converted beams are then recorded on the camera. The measured interference patterns are then processed using the Fourier-transform method

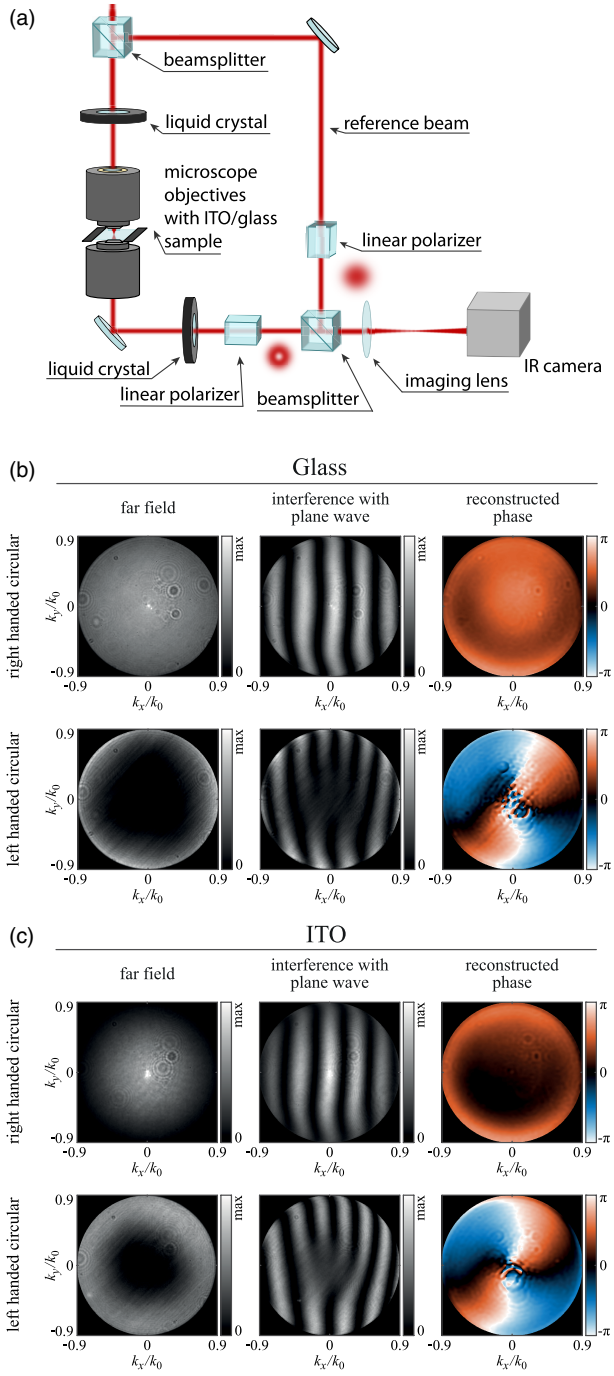

Fig. 3. (a) Experimental setup. (b) Images of the measured intensity and phase profiles in transmission for an incident RCP beam on an uncoated glass coverslip. (c) Corresponding intensity and phase profiles measured for a 310 nm thick ITO film on top of a glass coverslip at ENZ wavelength $\lambda = 1240$ nm.

introduced by Takeda *et al*. [44]. As a result, the phase profiles are retrieved from their corresponding interference patterns.

To verify the effect, three experiments were performed. In the first set of experiments, the polarization conversion was measured along with the intensity and phase profiles of the output beam by following the procedures described above using an uncoated glass coverslip. The bare glass coverslip shows that spin-to-orbit conversion can be achieved using a generic interface. Figure 3(b) shows for an incident RCP Gaussian beam the far-field intensities,

interference patterns, and corresponding phase profiles for both the transmitted RCP and LCP field components from the glass coverslip. The RCP component maintains its initial Gaussian intensity distribution and flat phase profile. The newly generated LCP component, however, carries an intensity singularity and a helical phase front. The presence of two fork dislocations in the interference fringe and the two 2π windings in the reconstructed phase confirms that the generated OAM beam has a topology $l = 2$.

In the second set of experiments, intensity and phase profile measurements of the output beam were taken for a 310 nm thick ITO layer on a glass substrate [Fig. 3(c)]. Similar to the glass coverslip, we also observe the generation of an OAM component for the case of an ITO film. A qualitative comparison between the ITO and the bare glass can already be made. While both ITO and glass show a converted OAM mode with left-handed circular polarization, the relative intensity for the ITO is much stronger compared to its glass counterpart. This indicates that the spin–orbit coupling for the ITO is more efficient than for the pure glass system.

The third set of measurements taken involve probing the spectral properties of the angular-dependent conversion of the ITO film. These measurements investigate two interesting behaviors. First, the spectral dependence shows the effect of an ENZ environment enhancing the spin–orbit interaction. Second, the angular dependence proves that the beam's nonparaxiality maximizes the conversion efficiency. The conversion efficiency is defined here as the ratio of the converted OAM beam to the total transmitted intensity of the beam. For the case of an incident RCP beam producing an LCP component with OAM, its conversion efficiency simply has the form $C = \frac{I_{\mathrm{LCP}}}{I_{\mathrm{RCP}}+I_{\mathrm{LCP}}}$, where I_{LCP} and I_{RCP} are the intensity values of the left-handed circularly and right-handed circularly polarized components of the transmitted light, respectively.

Due to indeterminable losses from the objective lens and the sample, the conversion efficiency considers only the total intensity of the transmitted beam and not the incident beam. The experimental results are compared with the generalized Fresnel transmission calculations [45] for a 310 nm thick ITO film in a three-medium system (air–ITO–glass), which follows the expression

$$t_{\mathrm{TE,TM}} = \frac{t^{(1,2)}_{\mathrm{TE,TM}} t^{(2,3)}_{\mathrm{TE,TM}} \exp(ik_{z2}d)}{1 + r^{(1,2)}_{\mathrm{TE,TM}} r^{(2,3)}_{\mathrm{TE,TM}} \exp(2ik_{z2}d)}.$$

Here $t_{\mathrm{TE,TM}}$ and $r_{\mathrm{TE,TM}}$ are the complex transmission and reflection Fresnel coefficients for both TE and TM components, respectively. Superscripts 1,2, and 3 represent the interfaces for the three media belonging to air, ITO, and glass, respectively. The coefficients additionally feature a propagator term for the fields in the ITO, which depend on the wavenumber along the propagation direction, k_{z2}, and the thickness of the ITO d.

For the bare glass coverslip, no spectral measurements were performed, because in good approximation, the refractive index of bare glass has a flat dispersion. Therefore, all conversion efficiencies for glass are treated only as a function of angle of incidence. Integrating the complete available angular spectrum up to an NA of 0.9, theory predicts a conversion efficiency for glass that is practically zero (0.06%). Such small values are below the sensitivity of the utilized experimental setup, which retrieved a value of 1.4%.

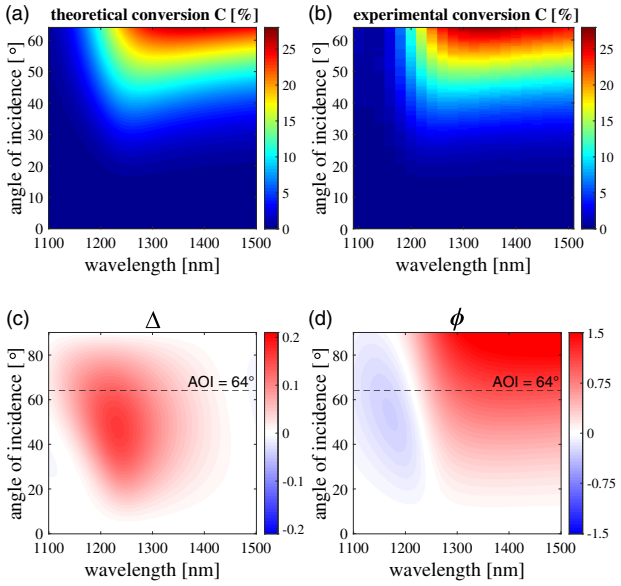

Fig. 4. (a) Theoretical conversion efficiency calculated from Fresnel transmission coefficients for an air–ITO–glass system. (b) Experimental transmission conversion efficiency measured for an incident RCP beam on a 310 nm thick ITO film with a glass substrate. The conversion efficiency is maximized when a higher NA is used for illuminating the interface. The higher NA increases the angle of incidence, allowing the maximum value from the contrasting Fresnel coefficients to be obtained. (c) The difference in magnitude Δ peaks around λ_{ENZ} and increases with angle of incidence to the ITO interface, where its maximum occurs around 47°, corresponding to roughly an NA of 0.73. (d) The phase difference ϕ carries a zero crossing near λ_{ENZ} followed by a strong difference for longer wavelengths. This phase difference contributes to the dephasing that the incident field incurs, adding to the spin–orbit interaction.

This small residual value can be attributed to measurement errors arising from the optical elements in the setup.

To observe the effect of an ENZ environment boosting the spin–orbit interaction, a set of wavelength-dependent measurements in the range of 1100 nm to 1500 nm was performed to measure the conversion efficiencies' spectral dependence (Fig. 4). At a wavelength of 1100 nm and an NA of 0.9 (64° angle of incidence), the permittivity of ITO is $0.8 + 0.24i$ and the conversion efficiency is approximately 1% for an incident RCP beam. The conversion efficiency steadily increases as the laser is tuned to a longer wavelength and reaches a maximum. The conversion efficiency for the ITO film peaks at 27.5%, however not at the zero-crossing wavelength of 1240 nm but at a longer wavelength of 1320 nm, where $\epsilon = -0.48 + 0.42i$.

Figures 4(a) and 4(b) further show that the ITO also enables rather high conversion efficiencies for wavelengths well above the ENZ wavelength. This spectral property is rooted in the complex nature of the Fresnel coefficients. Since the fundamental mechanism behind the spin–orbit coupling involves scaling and dephasing orthogonally polarized field components (TE and TM), then naturally the ITO's complex permittivity, along with its zero-crossing, will directly impact this effect. With this in mind, the influence of the complex-valued Fresnel coefficients can be assessed by looking at their difference in magnitude: $\Delta := |t_{\mathrm{TE}}| - |t_{\mathrm{TM}}|$, and their phase difference: $\phi := \mathrm{angle}(t_{\mathrm{TE}}/t_{\mathrm{TM}})$, where the angle function takes the relative phase difference between t_{TE} and t_{TM}. Around the ENZ wavelength, the differing Fresnel coefficients

carry little phase difference, and the predominance of the converted field is due primarily to Δ [Fig. 4(c)]. When the phase difference is effectively null, the maximum conversion efficiency occurs near the ENZ wavelength and an angle of incidence of approximately 47°. For longer wavelengths beyond λ_{ENZ}, the ITO behaves as a metal rather than an ENZ medium, and consequently, the phase difference between the two Fresnel coefficients becomes substantial [Fig. 4(d)]. Therefore, this mechanism contributes constructively to the total spin–orbit interaction by further strengthening the dephasing between the TE and TM components of the field. Since both Δ and ϕ contribute to the conversion efficiency of the generated OAM mode, the maximum contribution occurs above the ENZ wavelength where there is the strongest overlap between Δ and ϕ.

4. CONCLUSION

It has been demonstrated that the spin-to-OAM conversion that occurs for a circularly polarized beam incident on a planar interface can be enhanced in an ENZ environment, providing conversion efficiencies many times over conventional materials such as glass. Experimental results show that the spin-to-orbit conversion efficiency for ITO at an NA of 0.9 is 27.5% at a wavelength of 1320 nm, close to the theoretical prediction of 26.2% at 1367 nm. The strong spin–orbit coupling in ITO occurs due to the significantly contrasting Fresnel coefficients present in an ENZ setting, which contributes to the conversion efficiency of the generated OAM mode. It was also shown that the process is further strengthened when the incident field is tightly focused, allowing for a higher angle of incidence to increase the difference between t_{TE} and t_{TM}, thus scaling the amplitude of the converted mode. Furthermore, the complex Fresnel coefficients of ITO above the ENZ wavelength display a significant phase difference that consequently allows for a substantial conversion efficiency to be maintained even for longer wavelengths beyond λ_{ENZ}. Such findings have direct implications in the nonlinear propagation of optical beams in an ENZ medium, for ENZ-based beam shaping, and for designing ENZ-based metasurfaces or nanophotonic devices that exploit spin–orbit interactions. We also note that the large nonlinearity typically associated with an ENZ medium could be used to introduce dynamic control of the spin-to-orbit coupling in nanophotonics [39].

Funding. University of Graz; Natural Sciences and Engineering Research Council (Banting postdoctoral fellowship).

Acknowledgment. The authors acknowledge the financial support by the University of Graz. R.F. acknowledges the financial support of the Banting postdoctoral fellowship of the NSERC.

Disclosures. The authors declare no conflicts of interest.

Data Availability. Data underlying the results presented in this paper are not publicly available at this time but may be obtained from the authors upon reasonable request.

REFERENCES

1. R. A. Beth, "Mechanical detection and measurement of the angular momentum of light," Phys. Rev. **50**, 115 (1936).
2. L. Allen, S. Barnett, and M. Padgett, *Optical Angular Momentum* (CRC Press, 2016).
3. L. Allen, M. W. Beijersbergen, R. J. C. Spreeuw, and J. P. Woerdman, "Orbital angular momentum of light and the transformation of Laguerre-Gaussian laser modes," Phys. Rev. A **45**, 8185–8189 (1992).
4. K. Y. Bliokh, F. Rodrguez-Fortuño, F. Nori, and A. V. Zayats, "Spin–orbit interactions of light," Nat. Photonics **9**, 796–808 (2015).
5. A. T. O'Neil, I. MacVicar, L. Allen, and M. J. Padgett, "Intrinsic and extrinsic nature of the orbital angular momentum of a light beam," Phys. Rev. Lett. **88**, 053601 (2002).
6. N. B. Simpson, K. Dholakia, L. Allen, and M. J. Padgett, "Mechanical equivalence of spin and orbital angular momentum of light: an optical spanner," Opt. Lett. **22**, 52–54 (1997).
7. H. He, M. E. J. Friese, N. R. Heckenberg, and H. Rubinsztein-Dunlop, "Direct observation of transfer of angular momentum to absorptive particles from a laser beam with a phase singularity," Phys. Rev. Lett. **75**, 826–829 (1995).
8. H. Rubinsztein-Dunlop, A. Forbes, M. V. Berry, M. R. Dennis, D. L. Andrews, M. Mansuripur, C. Denz, C. Alpmann, P. Banzer, T. Bauer, E. Karimi, L. Marrucci, M. Padgett, M. Ritsch-Marte, N. Litchinitser, N. Bigelow, C. Rosales-Guzmán, A. Belmonte, J. Torres, T. Neely, M. Baker, R. Gordon, A. Stilgoe, J. Romero, A. G. White, R. Fickler, A. Willner, G. Xie, B. McMorran, and A. Weiner, "Roadmap on structured light," J. Opt. **19**, 013001 (2016).
9. E. Brasselet, Y. Izdebskaya, V. Shvedov, A. S. Desyatnikov, W. Krolikowski, and Y. S. Kivshar, "Dynamics of optical spin-orbit coupling in uniaxial crystals," Opt. Lett. **34**, 1021–1023 (2009).
10. P. Banzer, U. Peschel, S. Quabis, and G. Leuchs, "On the experimental investigation of the electric and magnetic response of a single nano-structure," Opt. Express **18**, 10905–10923 (2010).
11. A. Mair, A. Vaziri, G. Weihs, and A. Zeilinger, "Entanglement of the orbital angular momentum states of photons," Nature **412**, 313–316 (2001).
12. J. Wang, J.-Y. Yang, I. M. Fazal, N. Ahmed, Y. Yan, H. Huang, Y. Ren, Y. Yue, S. Dolinar, M. Tur, and A. E. Willner, "Terabit free-space data transmission employing orbital angular momentum multiplexing," Nat. Photonics **6**, 488–496 (2012).
13. N. Bozinovic, Y. Yue, Y. Ren, M. Tur, P. Kristensen, H. Huang, A. E. Willner, and S. Ramachandran, "Terabit-scale orbital angular momentum mode division multiplexing in fibers," Science **340**, 1545–1548 (2013).
14. M. Erhard, R. Fickler, M. Krenn, and A. Zeilinger, "Twisted photons: new quantum perspectives in high dimensions," Light Sci. Appl. **7**, 17146 (2018).
15. J. Leach, B. Jack, J. Romero, A. K. Jha, A. M. Yao, S. Franke-Arnold, D. G. Ireland, R. W. Boyd, S. M. Barnett, and M. J. Padgett, "Quantum correlations in optical angle–orbital angular momentum variables," Science **329**, 662–665 (2010).
16. S. W. Hell and J. Wichmann, "Breaking the diffraction resolution limit by stimulated emission: stimulated-emission-depletion fluorescence microscopy," Opt. Lett. **19**, 780–782 (1994).
17. F. Manni, K. G. Lagoudakis, T. Paraso, R. Cerna, Y. Léger, T. C. H. Liew, I. Shelykh, A. V. Kavokin, F. Morier-Genoud, and B. Deveaud-Plédran, "Spin-to-orbital angular momentum conversion in semiconductor microcavities," Phys. Rev. B **83**, 241307 (2011).
18. M. W. Beijersbergen, L. Allen, H. Van der Veen, and J. Woerdman, "Astigmatic laser mode converters and transfer of orbital angular momentum," Opt. Commun. **96**, 123–132 (1993).
19. M. Beijersbergen, R. Coerwinkel, M. Kristensen, and J. Woerdman, "Helical-wavefront laser beams produced with a spiral phaseplate," Opt. Commun. **112**, 321–327 (1994).
20. V. Y. Bazhenov, M. Soskin, and M. Vasnetsov, "Screw dislocations in light wavefronts," J. Mod. Opt. **39**, 985–990 (1992).
21. A. M. Yao and M. J. Padgett, "Orbital angular momentum: origins, behavior and applications," Adv. Opt. Photon. **3**, 161–204 (2011).
22. L. Marrucci, C. Manzo, and D. Paparo, "Optical spin-to-orbital angular momentum conversion in inhomogeneous anisotropic media," Phys. Rev. Lett. **96**, 163905 (2006).
23. E. Karimi, B. Piccirillo, L. Marrucci, and E. Santamato, "Light propagation in a birefringent plate with topological charge," Opt. Lett. **34**, 1225–1227 (2009).
24. A. Niv, Y. Gorodetski, V. Kleiner, and E. Hasman, "Topological spin-orbit interaction of light in anisotropic inhomogeneous subwavelength structures," Opt. Lett. **33**, 2910–2912 (2008).
25. R. C. Devlin, A. Ambrosio, N. A. Rubin, J. B. Mueller, and F. Capasso, "Arbitrary spin-to–orbital angular momentum conversion of light," Science **358**, 896–901 (2017).
26. T. A. Nieminen, A. B. Stilgoe, N. R. Heckenberg, and H. Rubinsztein-Dunlop, "Angular momentum of a strongly focused Gaussian beam," J. Opt. A **10**, 115005 (2008).

27. Y. Zhao, J. S. Edgar, G. D. Jeffries, D. McGloin, and D. T. Chiu, "Spin-to-orbital angular momentum conversion in a strongly focused optical beam," Phys. Rev. Lett. **99**, 073901 (2007).
28. K. Y. Bliokh, E. A. Ostrovskaya, M. A. Alonso, O. G. Rodrguez-Herrera, D. Lara, and C. Dainty, "Spin-to-orbital angular momentum conversion in focusing, scattering, and imaging systems," Opt. Express **19**, 26132–26149 (2011).
29. S. Nechayev, J. S. Eismann, G. Leuchs, and P. Banzer, "Orbital-to-spin angular momentum conversion employing local helicity," Phys. Rev. B **99**, 075155 (2019).
30. W. Nasalski, "Polarization versus spatial characteristics of optical beams at a planar isotropic interface," Phys. Rev. E **74**, 056613 (2006).
31. M. Yavorsky and E. Brasselet, "Polarization and topological charge conversion of exact optical vortex beams at normal incidence on planar dielectric interfaces," Opt. Lett. **37**, 3810–3812 (2012).
32. R. Barczyk, S. Nechayev, M. A. Butt, G. Leuchs, and P. Banzer, "Vectorial vortex generation and phase singularities upon Brewster reflection," Phys. Rev. A **99**, 063820 (2019).
33. I. Liberal and N. Engheta, "Near-zero refractive index photonics," Nat. Photonics **11**, 149–158 (2017).
34. O. Reshef, I. De Leon, M. Z. Alam, and R. W. Boyd, "Nonlinear optical effects in epsilon-near-zero media," Nat. Rev. Mater. **4**, 535–551 (2019).
35. J. Wu, Z. T. Xie, Y. Sha, H. Fu, and Q. Li, "Epsilon-near-zero photonics: infinite potentials," Photon. Res. **9**, 1616–1644 (2021).
36. N. Engheta, "Pursuing near-zero response," Science **340**, 286–287 (2013).
37. R. W. Ziolkowski, "Propagation in and scattering from a matched metamaterial having a zero index of refraction," Phys. Rev. E **70**, 046608 (2004).
38. M. Silveirinha and N. Engheta, "Tunneling of electromagnetic energy through subwavelength channels and bends using ε-near-zero materials," Phys. Rev. Lett. **97**, 157403 (2006).
39. M. Z. Alam, I. De Leon, and R. W. Boyd, "Large optical nonlinearity of indium tin oxide in its epsilon-near-zero region," Science **352**, 795–797 (2016).
40. A. Alu, M. G. Silveirinha, A. Salandrino, and N. Engheta, "Epsilon-near-zero metamaterials and electromagnetic sources: tailoring the radiation phase pattern," Phys. Rev. B **75**, 155410 (2007).
41. Z. Xu and H. F. Arnoldus, "Reflection by and transmission through an ENZ interface," OSA Contin. **2**, 722–735 (2019).
42. N. Radwell, R. Hawley, J. Götte, and S. Franke-Arnold, "Achromatic vector vortex beams from a glass cone," Nat. Commun. **7**, 10564 (2016).
43. A. Ciattoni, A. Marini, and C. Rizza, "Efficient vortex generation in subwavelength epsilon-near-zero slabs," Phys. Rev. Lett. **118**, 104301 (2017).
44. M. Takeda, H. Ina, and S. Kobayashi, "Fourier-transform method of fringe-pattern analysis for computer-based topography and interferometry," J. Opt. Soc. Am. **72**, 156–160 (1982).
45. L. Novotny, "Allowed and forbidden light in near-field optics. I. A single dipolar light source," J. Opt. Soc. Am. A **14**, 91–104 (1997).